

Faulting Induced by Forced Fluid Injection and Fluid Flow Forced by Faulting: An Interpretation of Hydraulic-Fracture Microseismicity, Carthage Cotton Valley Gas Field, Texas

by J. T. Rutledge, W. S. Phillips, and M. J. Mayerhofer

Abstract We analyzed precisely located microearthquake data detected during five hydraulic fracture treatments in the Carthage gas field of east Texas. The treatments were conducted in two adjacent boreholes within interbedded sands and shales of the Upper Cotton Valley formation. The microearthquakes were induced within narrow horizontal bands that correspond to the targeted sandstone layers. Events throughout all the treatments show strike-slip faulting occurring uniformly along vertical fractures trending close to maximum horizontal stress direction. These events are consistent with the reservoir's prevalent natural fractures, known to be isolated within the sands and trending subparallel to the expected hydraulic fracture orientation. When this uniform fracture system was activated exclusively, the detected shear deformation, measured as the moment release per unit volume of fluid injected, was constant, independent of various fluid viscosities and flow rates used. Within the base of the Upper Cotton Valley formation, anomalous event counts and moment release occurred within dense clusters that delineate bends or jogs in the fracture zones. The mechanisms are also strike-slip, but the fault planes are more favorably oriented for failure. The dense clusters show location patterns diverging in time, suggesting the expulsion of fluids from compressive fault jogs. Fluid flow forced by the adjacent slip-induced loading appears to initially extend the treatments, but the loading also tends to lock up and concentrate stress at the jogs, as evident by fewer but larger events populating the structures as treatments progress. As a result, effective drainage lengths from the boreholes may be shorter than would be inferred from the seismicity extending past the jogs. These high-moment asperities are similar to dense patches of seismicity observed along creeping sections of the San Andreas fault, where they have been attributed to localized zones of strength or stress concentration, surrounded by larger regions undergoing stable, aseismic slip. This similarity, plus large moment deficits in terms of volume injected, suggests a large component of aseismic slip is induced by the Cotton Valley treatments.

Introduction

Microseismic monitoring is a technique used to image the volume of rock stimulated by hydraulic fracturing (Albright and Pearson, 1982). Seismometers are placed in boreholes near injection depths to detect and locate the induced microearthquakes. The method has been applied in developing hot dry rock reservoirs (e.g., Pine and Batchelor, 1984; House, 1987; Jones *et al.*, 1995; Tezuka and Niitsuma, 2000) and has been demonstrated in oil and gas fields as a technique for mapping and calibrating stimulations (e.g., Phillips *et al.*, 1998; Warpinski *et al.*, 1998), monitoring waste injection (Keck and Withers, 1994), and delineating reservoir structures affected by production (e.g., Rutledge *et al.*,

1998). Applications are becoming more routine with the availability of retrievable borehole receiver arrays (e.g., Dyer *et al.*, 1999; Maxwell *et al.*, 2002; Griffin *et al.*, 2003). Beyond mapping gross structure and fluid-flow paths, relative source location techniques can also be applied to reservoir microseismicity to resolve discrete fracture geometry and aid in solving source mechanisms (e.g., Phillips *et al.*, 1997; Phillips, 2000; Fehler *et al.*, 2001; Rowe *et al.*, 2002; Moriya *et al.*, 2003), thereby providing more detailed information on how the forced fluid flow affects a reservoir's natural fractures. More generally, seismicity induced in hydrocarbon and geothermal fields can provide field-scale en-

vironments in which the interactions of faulting and fluid flow can be studied under controlled operations and where geology is well known (Pennington *et al.*, 1986).

In 1997, a consortium of oil field operators and service companies conducted a series of hydraulic fracture imaging tests in the Carthage Cotton Valley gas field of east Texas (Walker, 1997). Microseismic data were collected and processed for six hydraulic fracture treatments in two wells (three completion intervals per well) (Mayerhofer *et al.*, 2000). The reservoir is typical of low-permeability gas resources that require hydraulic-fracture stimulation for economic production. One well was completed with gel-proppant treatments in which a viscous crosslinked gel was injected to carry high concentrations of sand proppant into formation. The second well was completed using treated water and low proppant concentrations (waterfracs). Waterfracs have been shown to be just as effective as the conventional gel-proppant treatments in Cotton Valley reservoirs, but at greatly reduced cost (Mayerhofer *et al.*, 1997). Reasons suggested for the success of waterfracs include (1) induced shear displacement along natural and hydraulic fractures results in self-propping (shear dilation enhanced by fracture branching, proppant, and spalled rock fragments), (2) fracture extension and the removal of treatment fluids that might impede production are both easier to achieve with low-viscosity fluids, and (3) damage to fracture conductivity caused by gels is reduced (Mayerhofer and Meehan, 1998). To understand and characterize the rock's mechanical responses that may have enhanced or diminished permeability in the Carthage gas field, we have taken a detailed look at the microseismicity induced by the two treatment types. Our analysis includes improving relative source locations, determining focal mechanisms, comparing the seismic moment released by the various injections, and examining the space-time patterns of event occurrence.

Operational Setup

The treatment and monitor wells are shown in Figure 1. Two multilevel, three-component geophone arrays were attached to the outside of 2½-inch production tubing and cemented into the monitor wells 21-09 and 22-09 (for details see Walker, 1997). We refer to these as array 1 and array 2 (Fig. 1). We used data from the subset of geophones shown in Figure 1, which span the completion zones and the entire operating lengths of the arrays.

Well 21-10 was completed with gel-proppant treatments and was monitored using both arrays. Afterward well 21-09 was completed by waterfrac and monitored using array 2 only. We present the monitoring results of five treatments (A–E, Table 1) covering common stratigraphic intervals within the Upper Cotton Valley formation (UCV). The UCV is an approximately 250-m-thick sequence of interbedded sands, siltstones, and shales (for details see Walker, 1997). The well casings were perforated over 3- to 6-m intervals to target discrete productive sand horizons. Multiple intervals

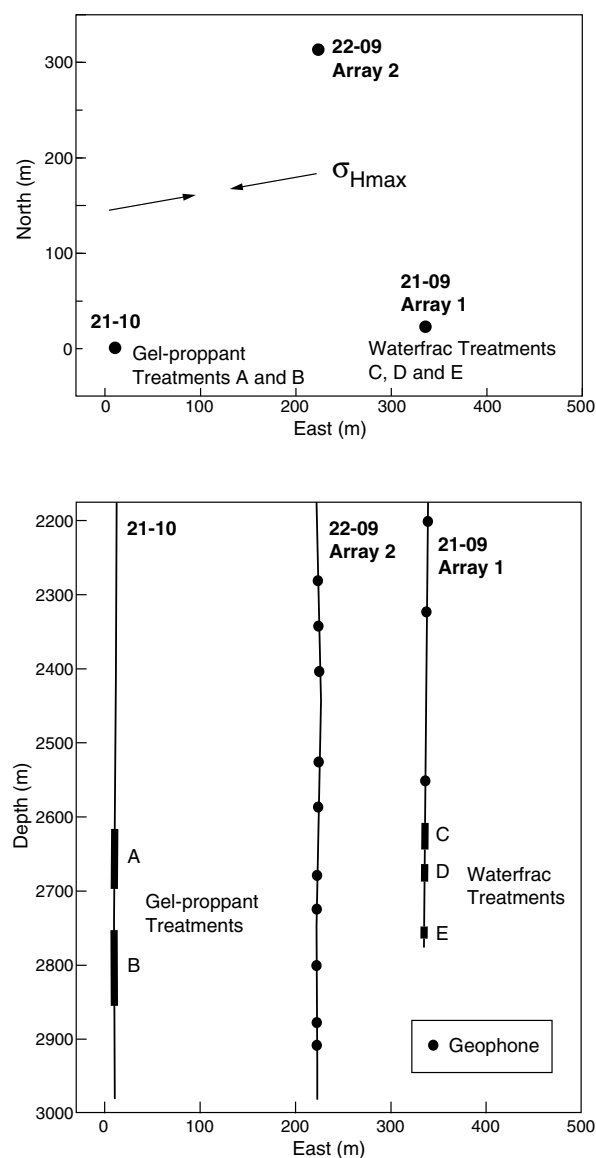


Figure 1. Treatment and monitor wells in plan and depth view. The approximate direction of maximum horizontal stress (σ_{Hmax}) for the region at reservoir depth is shown (Laubach and Monson, 1988). The treatment intervals are marked by the heavier lines along the boreholes. Each of these treatment intervals comprises a series of discrete perforation intervals, 3 to 6 m long, that targets specific sand intervals (Table 1). Datum for all maps herein is the kelly bushing of well 21-10 at 119 m above sea level.

were simultaneously treated (Table 1). The fluid used in the waterfracs is a low-viscosity linear gel, referred to as treated water (Table 1). UCV waterfracs are typically pumped at 130 to 160 l/sec (50 to 60 barrels per minute [bbl/min]), but pressure limitations and the small-diameter casing in well 21-09 restricted the waterfrac injection rates to 26.5 l/sec (10 bbl/min). The low flow rates in 21-09 also required shorter depth intervals to be treated separately, and total slurry volumes (fluid and sand) were reduced to about two-

Table 1
Hydraulic Fracture Treatment Data within the Upper Cotton Valley Formation

	Treatment and Depth Interval	Target Sand Units	Total Perforation Interval	Total Slurry Volume	Total Proppant	Injection Rate
Well 21-10, gel proppant	A 2615–2696 m	D-sand, Bodcaw, Vaughn, Davis, Bolinger	24 m (80 ft)	1340 m ³ (8428 bbl)	228,634 kg (503,600 lb)	119 l/sec (45 bbl/min)
Cross-linked gel polymer concentration: 25 lb/1000 gal Viscosity: 150 cP at 250°F	B 2757–2838 m	E-sand, Justiss, Ardis, Roseberry	24 m (80 ft)	1253 m ³ (7881 bbl)	190,680 kg (420,000 lb)	106 l/sec (40 bbl/min)
Well 21-09, waterfrac	C 2607–2643 m	D-sand, Bodcaw	12 m (40 ft)	419 m ³ (2635 bbl)	14,891 kg (32,800 lb)	26.5 l/sec (10 bbl/min)
Linear gel polymer concentration: 20 lb/1000 gal Viscosity: 3 to 4 cP at 250°F	D 2663–2687 m	Vaughn, Davis, Bolinger	12 m (40 ft)	396 m ³ (2491 bbl)	12,394 kg (27,300 lb)	26.5 l/sec (10 bbl/min)
	E 2746–2763 m	E-sand, Justiss	9 m (30 ft)	400 m ³ (2516 bbl)	7264 kg (16,000 lb)	21.2 to 26.5 l/sec (8 to 10 bbl/min)

thirds of the 21-10 treatments per unit depth interval (Table 1 and Fig. 1). As a result, the waterfrac injection rates per unit depth interval are reduced only twofold from the 21-10 gel-proppant treatments, but these rates are still unusually low. However, the 21-10 gel-proppant treatments are initiated with treated-water pumping stages, providing monitoring conditions closer to typical waterfrac injection rates.

Data Analysis

The initial microseismic maps are presented by Mayoher *et al.* (2000) and Urbancic and Rutledge (2000). We relocated the microearthquake sources with more precise arrival-time data obtained by systematic and consistent re-picking of events with similar waveforms. The relocation method and its application to treatment A (Table 1) are presented by Rutledge and Phillips (2003). On average, we reduced the standard deviation of arrival-time residuals fourfold to fivefold from the original pick data (from approximately 1.0 to 0.2 msec). The relative error ellipsoids for locations determined using both arrays (treatments A and B) have major axes generally oriented horizontal and orthogonal to the plane of the two monitor wells, with a mean length of 4 m (± 2 m). Average relative depth error is slightly less than ± 1 m. Location errors determined using array 2 only (treatments C, D, and E) are similar in depth, but larger in plan view due to uncertainty in particle motion data used to determine azimuth to source. The mean, relative azimuthal error for all single-array locations is $\pm 1^\circ$, based on the standard error of the mean azimuth obtained from six stations of array 2. This angular error corresponds to ± 6 m at interwell distances (~ 350 m). Absolute depth errors, attributed to velocity-model uncertainty, are as great as 4 m, based on misalignment of the source locations with the targeted (perforated) sand intervals (Rutledge and Phillips, 2003).

With the improved locations we solved composite focal

mechanisms for event groups, with grouping based on waveform similarity and discrete location clusters. We used Snoké's (2003) focal-mechanism routine with a combination of P and SH polarities and the amplitude ratios of SH/P , SV/P , and SV/SH as input to constrain the solutions.

We computed moment scalar values (M_0) using Andrews's (1986) technique, averaging values obtained from P and S phases recorded over several stations. Beforehand, we corrected P and S amplitudes for radiation patterns based on the focal mechanism solutions. In addition we adjusted P and S amplitudes for spreading and attenuation. The P - and S -wave spatial attenuation coefficients are both about 2×10^{-4} dB sec/m ($Q_p \sim 30$, $Q_s \sim 50$), based on amplitude decay measured across the receiver arrays (Rutledge, 1998).

Locations and Focal Mechanisms

Top of the UCV

Microseismic locations for the shallowest completion intervals of the UCV are displayed in Figure 2 (treatments A and C, Table 1). We have displayed only the eastern wing of treatment A because event detection rapidly falls off west of well 21-10 (Rutledge and Phillips, 2003). Events induced by both the gel-proppant and waterfrac treatments form long narrow zones only 8 to 12 m wide. Treatment lengths for the waterfrac are about two-thirds of the length attained by the gel-proppant treatment, proportional to the volumes per unit length of borehole treated (Table 1). The event trends are parallel at N80°E, close to independent measurements of maximum horizontal stress (σ_{Hmax}) direction (about N75°E to N85°E, Laubach and Monson, 1988). The depth views show nearly identical banding and distribution of event locations over their common depth intervals (Fig. 2). The banding correlates with the discrete perforation intervals (targeted sands) and zones of high-volume flow as indicated by proppant tracer logs run in the treatment wells (Rutledge and Phillips, 2003).

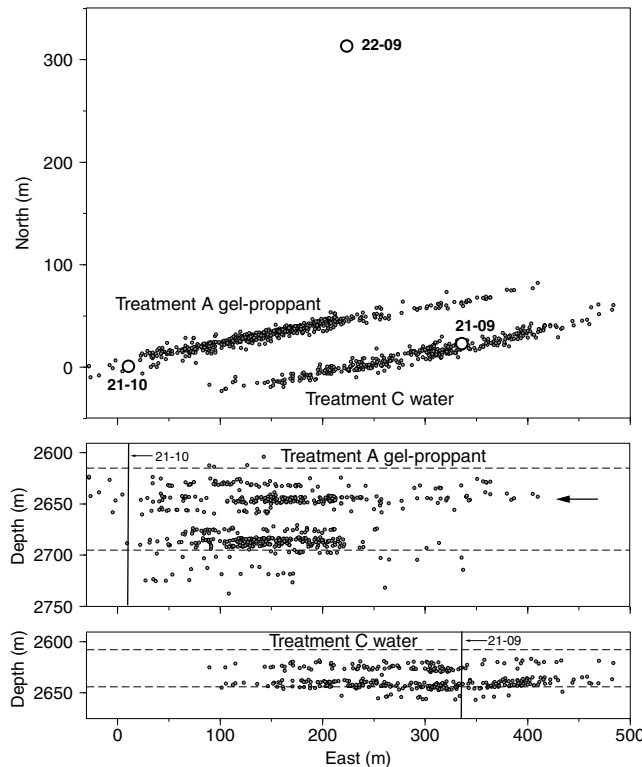


Figure 2. Source locations for gel-proppant and waterfrac treatments A and C within the top of the UCV. The tops and bottoms of the perforated intervals are marked with dashed lines in depth views. The arrow marks one of the most populous depth-band clusters of treatment A, which is displayed in greater detail in Figure 10.

Events from both treatments show similar waveforms for adjacent sources over their respective lengths. In addition, the P and SH polarities and amplitude ratios show nearly identical spatial patterns with respect to the common monitor well (array 2, Fig. 1). As shown for treatment A (Rutledge and Phillips, 2003), these data indicate two similar focal mechanisms occurring uniformly over the entire treatment lengths. The composite focal mechanisms indicate both left- and right-lateral strike-slip faulting along near-vertical fracture planes that strike subparallel with σ_{Hmax} (Fig. 3). First-motion and amplitude-ratio data for the waterfrac covering the lower interval of treatment A (treatment D, Table 1) also give the same two composite focal mechanisms (not shown). The banding of seismicity (Fig. 2) and the nodal planes trending close to the event trends (Fig. 3) are consistent with activation of the reservoir's prevalent natural fractures, a system of vertical fractures that are isolated within individual sands and that trend within 10° of expected hydraulic fracture orientation (Laubach, 1988; Dutton *et al.*, 1991). In all cases the majority of events fit left-lateral slip (85% to 90%), suggesting the predominant fracture trend is slightly clockwise of σ_{Hmax} . The relative error ellipsoids indicate that the widths of the active fracture zones are signifi-

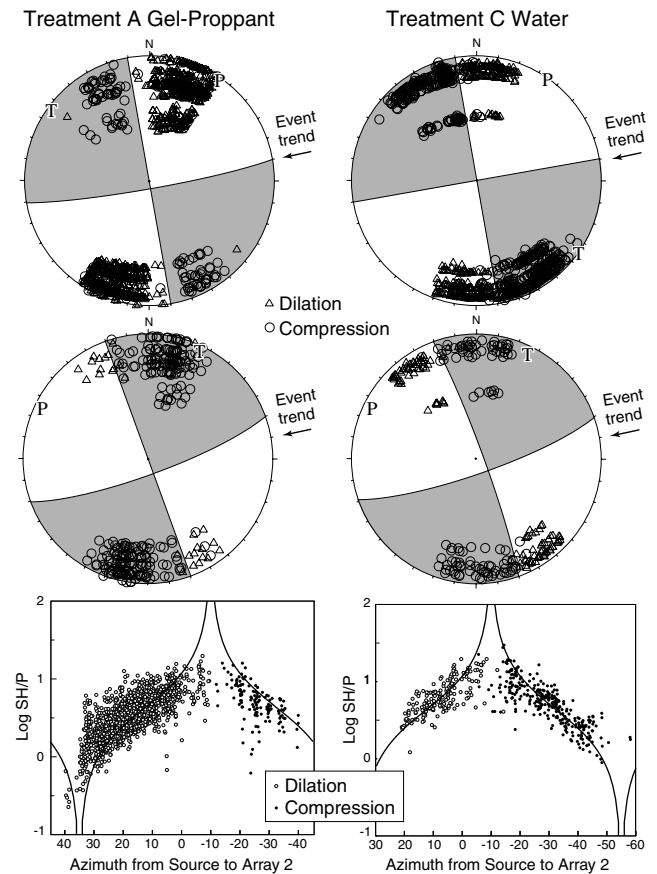


Figure 3. Composite focal mechanisms for the treatments shown in Figure 2. Solutions are constrained by P and SH first motions as well as amplitude ratios SH/P , SV/P , and SV/SH . The SH/P versus azimuth from source to receiver for the more populous subsets fitting left-lateral slip is shown below the focal mechanisms. All nondiscrepant P polarities are also distinguished on the SH/P displays ($>95\%$ of all events). The curves on the SH/P displays are the theoretical amplitude ratios for a vertical, strike-slip fault striking $N80^\circ E$ at horizontal takeoff angle.

cant, hence we infer that narrow zones of multiple, subparallel fractures are pressurized (Rutledge and Phillips, 2003).

Base of the UCV

Event locations and focal mechanisms for the treatments within the base of the UCV are displayed in Figures 4–6 (treatments B and E, Table 1). Similar to the shallower zones, the seismicity is banded corresponding to isolated sand intervals (Figs. 4 and 6). However, anomalously high event counts are induced at these depths within small clusters that strike off angle from the overall treatment trends of $N80^\circ E$. For the gel-proppant treatment, clusters 1 to 4 account for 65% of the events detected, and cluster 4 alone makes up 42% (Fig. 4). Similarly, for the waterfrac, 80% of the events occur within the easternmost cluster (cluster 5, Fig. 6). Focal mechanisms for the off-trend clusters also show strike-slip faulting, but the slip planes are more opti-

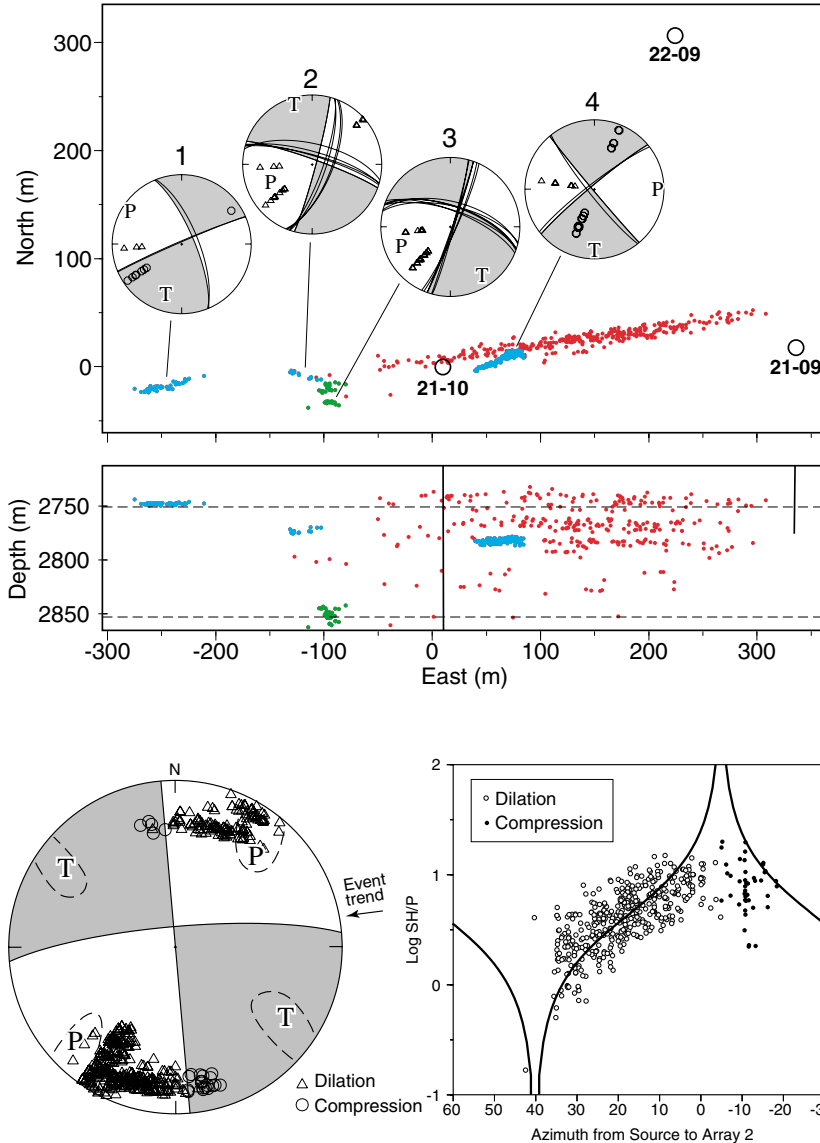


Figure 4. Source locations and subcluster focal mechanism for gel-proppant treatment B at base of the UCV. The four subclusters shown in blue and green account for 65% of all events detected; cluster 4 alone accounts for 42%. Slip planes and event-trend orientations for the four subclusters strike off-angle from the overall treatment trend delineated by the red events. A composite focal mechanism for the red events is displayed in Figure 5.

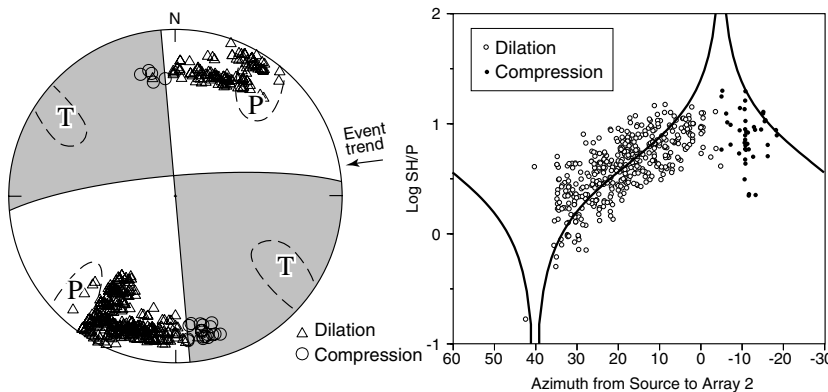


Figure 5. Focal mechanism and SH/P amplitude distribution for 64% of the events shown red in Figure 4. Grouping was based on SH and P polarities. Sixteen percent of the events shown in red on Figure 4 fit a similarly oriented, right-lateral solution; 20% fit neither. The curves on the SH/P display are the theoretical amplitude ratio distribution for a vertical strike-slip fault striking $N85^\circ E$ at horizontal takeoff angle.

mally oriented for failure, as indicated by the P and T axis trending close to the σ_{Hmax} and σ_{Hmin} directions. The other event locations, shown in red, are distributed more extensively and continuously along the treatment lengths at a less dense spacing (Figs. 4 and 6). Most of the red events fit strike-slip focal mechanisms similar to those of the top of the UCV (Fig. 3), with one nodal plane trending close to the σ_{Hmax} direction (Fig. 5 and cluster-2 mechanism of Fig. 6). M_0 distributions for these on-trend events at both depth intervals are similar and, on average, have M_0 values five times weaker than the off-trend clusters dominating the event counts at the base of the UCV. Because they are weaker, the on-trend events fall out of detection range on the west side of 21-10 (Rutledge and Phillips, 2003) and, we speculate, likely fill the gaps between the energetic off-trend clusters on the far side of the treatment well (Fig. 4).

Thus, seismicity induced within the deeper UCV indicates that a more heterogeneous population of natural frac-

tures is being pressurized. Summing the M_0 release of the various treatments underscores the dominance of seismic energy associated with the densely populated, off-trend clusters.

Cumulative Moment Release Per Unit Volume Injected

To compare the seismic deformation of the various treatments, we plot cumulative moment release (ΣM_0) versus cumulative volume injected (ΣV) (Fig. 7). ΣM_0 for natural seismicity has been shown to be proportional to slip rates on a given fault (Brune, 1968) or proportional to strain rates throughout some active volume (Scholz, 1990, and references therein). McGarr (1976) derived a model by which $\Sigma M_0 = K\mu\Delta V$, where μ is the shear modulus, K is a factor close to 1, and ΔV is a volume change for which it is assumed all associated strain is accommodated by seismic fail-

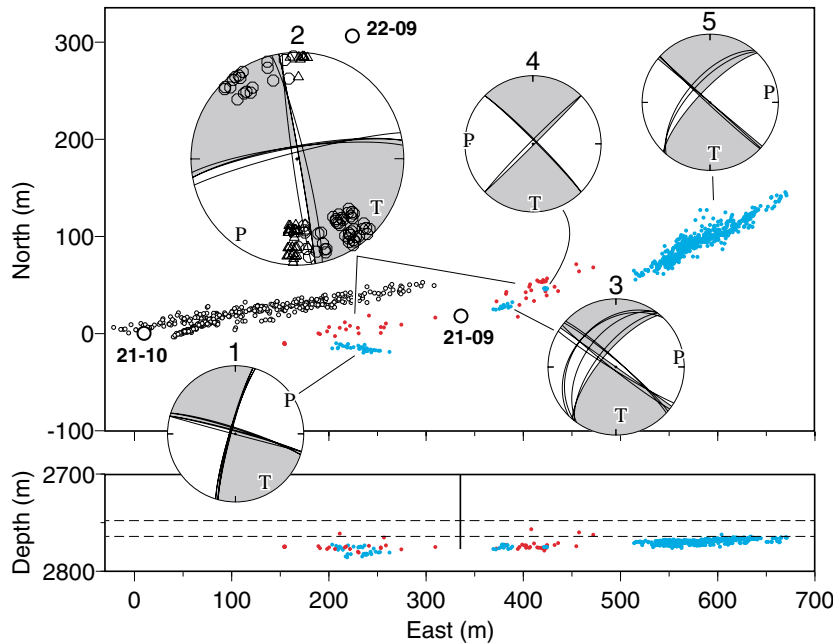


Figure 6. Source locations (red and blue) and focal mechanisms for waterfrac treatment E at base of UCV. For comparison of the event trends, the events of the eastern wing of treatment B are also shown as open symbols. The seismicity depth locations suggest most of the injectate found a permeable horizon near the well bottom (21-09). This depth zone corresponds to one of the most active zones stimulated in 21-10 (Fig. 4). Most of the red events fit the on-trend focal mechanism, shown larger (number 2). Clusters 1, 3, 4, and 5 are the more numerous and energetic events showing slip planes and event trends striking off-angle from the \sim N80°E trend.

ure. For hydraulic fracturing in oil and gas reservoirs, the ΔV corresponding to fluid injected would be seismically underestimated because of the fluid accommodated by rock porosity (McGarr, 1976). Indeed, in terms of McGarr's relationship, the curves of Figure 7 have slopes that are 3 to 4 orders of magnitude less than a reasonable μ for sandstone ($\sim 10^{10}$ N/m², [Birch, 1966]). ΣM_0 measured during hydraulic fracturing may be deficient in general. Fehler and Phillips (1991), for example, found a moment-release deficit during hydraulic fracturing in granitic rock, which they attribute to undetected small events that often dominate injection-induced seismicity (b -values are unusually high, similar to natural earthquake swarms). Further, hydraulic-fracture seismicity is mostly associated with fluids invading existing fractures that may open and slip aseismically, or at least result in signals with frequencies significantly lower than the detected shear events.

Because of detection-range bias, we summed the moments over the most populous wings of each treatment (east or west of the respective treatment well) and, as an approximation, doubled those ΣM_0 values for display in Figure 7, assuming symmetric seismicity about the treatment wells. The symmetry is not necessarily true and is less likely to be true at the base of the UCV where a more heterogeneous fracture system is activated (treatments B and E). Our approximation for treatment E, for example, overestimates the total moment release that would have been detected without a distance bias, since the seismicity is clearly asymmetric with 89% of the events located on the more distant wing, east of well 21-09 (Fig. 6). Rutledge and Phillips (2003) showed that seismicity west of well 21-10 was likely undersampled due to limited detection range, allowing the possibility that the on-trend events were symmetrically distributed about well 21-10. But, within the possibility that less

seismicity did occur west of 21-10, our approximation of doubling ΣM_0 will generally overestimate the detectable moment release.

In addition, we show as the dashed lines on Figure 7 a measure of the cumulative hydraulic energy imparted at the formation versus ΣV . We computed hydraulic energy as $P_n \times V$, where P_n is net pressure, defined as the estimated average pressure along the fracture length exceeding σ_{Hmin} (Gidley *et al.*, 1989). The hydraulic energy per unit volume injected, that is, the slopes of the dashed curves or P_n , are similar for the various treatments (Fig. 7), which allows us to attribute most of the differences in ΣM_0 to differences in structures activated. Table 2 summarizes the totals of ΣM_0 , $\Sigma M_0/\Sigma V$, and hydraulic energy, as well as the wings over which ΣM_0 were obtained.

Results of $\Sigma M_0/\Sigma V$

The most direct comparison we can make are the common intervals treated within the top of the UCV. We synchronized and combined the data for the waterfrac treatments C and D to correspond to the same depth interval as treatment A (Table 1). As noted above, the locations (Fig. 2) and first-motion and amplitude-ratio data (Fig. 3) indicate a similar and fairly uniform fracture system is activated for both treatment types within the top of the UCV. The slopes of the curves ($\Delta M_0/\Delta V$) for this common interval are near identical, independent of fluid type and injection rate (Fig. 7, treatments A and C + D).

The $\Delta M_0/\Delta V$ for the treatments within the base of the UCV are generally greater. Moment release on the east wing of treatment B is initially high (Fig. 7), associated with activity on the off-trend cluster 4 (Fig. 4). After about 500 m³ of fluid is injected, cluster 4 becomes quiescent and $\Delta M_0/\Delta V$ is reduced, running parallel to the shallower treatments

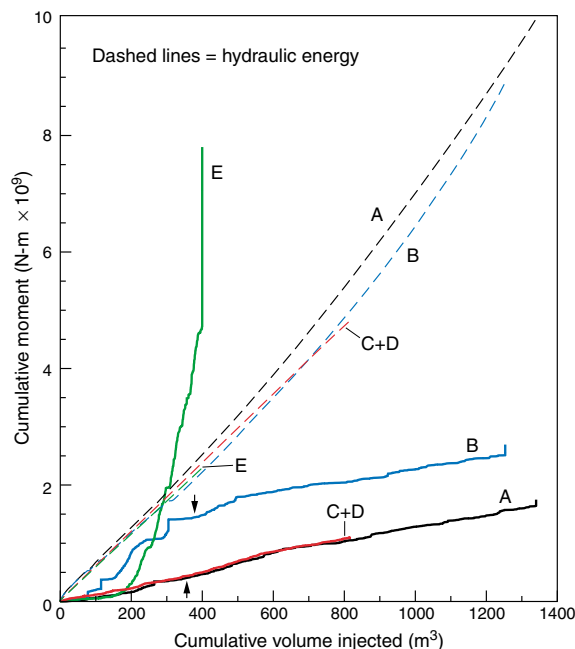


Figure 7. Cumulative moment release versus cumulative volume injected. To account for detection-range bias, ΣM_0 is computed over the most populous wing of each treatment (Table 2) and doubled to approximate total moment release. Treatments C and D were synchronized and combined to correspond to the same depth interval as A (Table 1). The arrows along gel-proppant treatments A and B mark the cumulative volumes at which the fluid was switched from the treated-water pumping stages to the cross-linked gel. The cumulative hydraulic energy imparted at the rock (dashed curves) is measured as $\Sigma(P_n \times V)$, where P_n is net pressure, defined as the estimated average pressure along the fracture length exceeding σ_{Hmin} . Hydraulic energy measured instead as pressures exceeding hydrostatic pressures at these depth intervals, would be 2.2 times the values displayed here.

A and C + D (Fig. 7). Activity east of the well after 500 m^3 is mostly due to the on-trend events, shown in red in Figure 4. Thus, the portion of $\Delta M_0/\Delta V$ of treatment B parallel to A and C + D corresponds to pressurizing a similar fracture system, as evident by the similarities of seismicity banding in depth and the composite focal mechanisms (Figs. 2–5).

The most anomalous seismic moment release occurred east of 21-09 during treatment E. For the last 200 m^3 pumped of treatment E, $\Delta M_0/\Delta V$ is about 40 times greater than for the on-trend fracture system activated within the top of UCV (Fig. 7). This anomaly is due to activation of cluster 5 (Fig. 6). Initially the $\Delta M_0/\Delta V$ is parallel to treatments A and C + D but quickly steepens after 160 m^3 of fluid is injected, when cluster 5 becomes active. This treatment also resulted in the largest seismic release following shut-in (injection stopped), continuing for at least 75 min and represented by the long vertical leg at the end of the ΣM_0 curve (Fig. 7). As we show next, the anomalous deformation detected within

the base of the UCV (treatments B and E) is due to structurally controlled stress heterogeneities, as evident from details of source locations, moment distribution, and growth patterns.

Anomalous Structures and Growth Patterns

Cluster 5 of treatment E was the most energetic structure activated (Fig. 6). Figure 8 shows a structural interpretation and the temporal development of this fracture zone. Most of the events and moment release occur near the bend or jog in the seismicity trend, at about 550–575 m east (Fig. 8). Activity also initiates within the jog at about 570 m east (Fig. 8), at least 100 m east of any other activity (Fig. 6), suggesting that this high-moment asperity may have been loaded by aseismic slip induced to the west. The event sequence shows evidence of the faulting hydraulically feeding back on the forced injection. Right-lateral motion is induced along the whole length of the structure (Fig. 8), so that the left-stepping jog forms a compressional zone in which mean stress should be increasing (Segall and Pollard, 1980). A smaller dilational jog, stepping rightward at about 610 m east, may act as a local pressure sink; it appears to initially impede and delay the seismicity's eastward movement. After a few minutes' lag in activity near minute 275, the seismicity rapidly extends east of the dilational jog. Fault-induced loading at the compressional jog should be impeding fluid flow and slip. At about minute 330, the operators reduced the flow rate and suspended proppant injection in response to an undesired pressure rise. Activity in the compressional jog appears to react to the reduced injection rate. The seismicity diverges west and east from the kink at 575 m, which is now populated by fewer but larger events. The jog may be closing, expelling fluid previously stored and, due to more restricted flow, contributing to the pressure rise continuing to the end of injection. Faulting induced by fluid flow forced out along the adjacent legs should further drive this secondary fluid source, similar to the concept of seismic pumping (e.g., Sibson, 1981). With shut-in, the jog further depopulates and westward migration toward the injection well accelerates (Fig. 8). A few large events occur in the jog after shut-in, suggesting that stress continues to build in the area as a result of slip further induced on each leg.

The next most energetic structure monitored was cluster 4, which dominated treatment B (Fig. 4). Figure 9 shows the cluster development through the three initial test stages of pumping, during which 85% of its events occurred. Similar to the cluster of Figure 8, the kink in the structure at 70 m east forms an asperity, where stress would be expected to build (e.g., Andrews, 1989) and where the event density and moment release are greatest (Fig. 9). The event sequence shows the structure developing westward (Fig. 9), forming what appears to be a dead-end path projecting out of the main trend of seismicity (Fig. 4). Activity starts after the first shut-in, suggesting that fluid is driven westward, back toward the treatment well, and into this off-trend fracture

Table 2
Summary of Seismic Moment Release and Hydraulic Energy Imparted into Rock by Injection

Treatment	Wing Summed for ΣM_0	$2 \times \Sigma M_0$ (N m)	Hydraulic Energy (N m)	$\frac{2 \times \Sigma M_0}{\Sigma V}$ (N/m ²)
Well 21-10, gel proppant				
A	East of 21-10	1.75×10^9	9.93×10^9	1.30×10^6
B	East of 21-10	2.69×10^9	8.84×10^9	2.15×10^6
Well 21-09, waterfrac				
C + D	West of 21-09	1.11×10^9	4.76×10^9	1.37×10^6
E	East of 21-09	7.80×10^9	2.25×10^9	19.52×10^6

zone due to closure along the main trend of seismicity (red events of Fig. 4). During the third pumping stage an intense 10-min episode of seismicity occurs at the kink. A close-up of this sequence shows repetitive, stationary sources of similar magnitude (inset, Fig. 9). The isolation of this repetitive subcluster strongly suggests that aseismic slip is hydraulically induced east of the kink and is reloading this relatively strong area of the fracture zone. The sequence also suggests fluid storage and expulsion at the fracture zone bend. That is, immediately after the third pumping stage (Fig. 9), the kink is fairly quiet while numerous events rapidly define the western leg of the structure. A compressional zone with a tendency to expel fluids should be formed near the fault bend by the right-lateral slip and the general westward migration of seismicity (see figure 18 of Sibson, 2001). Finally, there is a quiet zone at about 62 m that may represent a small dilational jog. The depth view suggests some vertical communication of fluids at this location; that is, the events step down and banding is better defined west of the seismic gap.

Treatments within the top of the UCV also show evidence of stress heterogeneities and the induced faulting feeding back on the injection. Figure 10 shows an example from one of the most populous seismicity bands of treatment A, occurring over a 10-m depth interval and marked by the arrow in Figure 2. Ninety percent of these events fit a left-lateral strike-slip motion. The event sequence shows the development during the main portion of the treatment. Activity is initially concentrated near the treatment tip and is characterized by many small events slowly moving eastward (~ 150 to 220 m east). At about minute 235 a relatively large event occurs at 200 m east. A few minutes later seismicity diverges west and east from the area previously active, with the east branch offset about 6 m to the south in plan view. The offset results in a compressional jog, similar to the structure illustrated in Figure 8. Again, the diverging pattern of the event sequence suggests that fluid stored in the area previously most active is then expelled, with the adjacent faulting further driving this secondary fluid source into compression (Fig. 10).

If the migration of events toward the injection well (westward from minutes 240 to 280, Fig. 10) is caused by fluids driven out of the area previously active (near 200 m east), it would require local, transient reversal of the pressure

gradient. Prior to seismicity extending past the jog, potential energy near 200 m east should be growing as the fracture zone is inflated. A local pressure high should be created within the compressive jog in response to the fault loading (e.g., Zhang and Sanderson, 1996; Nemcok *et al.*, 2002). The energy released and fluid expelled from minutes 240 to 280 may occur in a series of pulses as the jog area (the seismic pump) is incrementally loaded by adjacent faulting. Near minute 280 pressure rise levels off, the diverging pattern breaks up, and eastward growth slows, perhaps due to the load-induced restriction of flow at the jog. Proppant will also tend to build up at the jog, further impeding flow and fracture growth (e.g., Warpinski and Teufel, 1987). The fracture zone near 200 m continues to be a site of stress accumulation, as evident by the largest event of this depth zone occurring there late in the treatment, at about minute 320 (Fig. 10).

Discussion and Conclusions

Seismicity induced by gel-proppant and waterfrac treatments in the UCV formation show similar distributions of event locations and focal mechanisms for common depth intervals. In general, strike-slip faulting is induced within narrow, horizontal bands.

Within the top of the UCV, the strike-slip faulting is almost exclusively induced along vertical fractures trending close to σ_{Hmax} . The slip-plane orientations and the banding of events are consistent with activation of the reservoir's prevalent natural fractures, a system of fractures that are isolated within individual sands and trend subparallel to the expected hydraulic fracture orientation. The majority of events fit left-lateral slip (85% to 90%), suggesting that the predominant fracture trend is slightly clockwise of σ_{Hmax} .

Seismicity within the base of the UCV indicates that a more heterogeneous fracture system is pressurized. Most of the events and moment release occur within dense clusters that delineate bends or jogs in fault structures. The mechanisms are also strike-slip, but the fault planes of these clusters are more favorably oriented for failure. The remaining seismicity is similar to the top of the UCV, with generally weaker events more evenly populating long horizontal bands and slip vectors that trend close to the σ_{Hmax} direction.

The dense clusters within the base of the UCV show

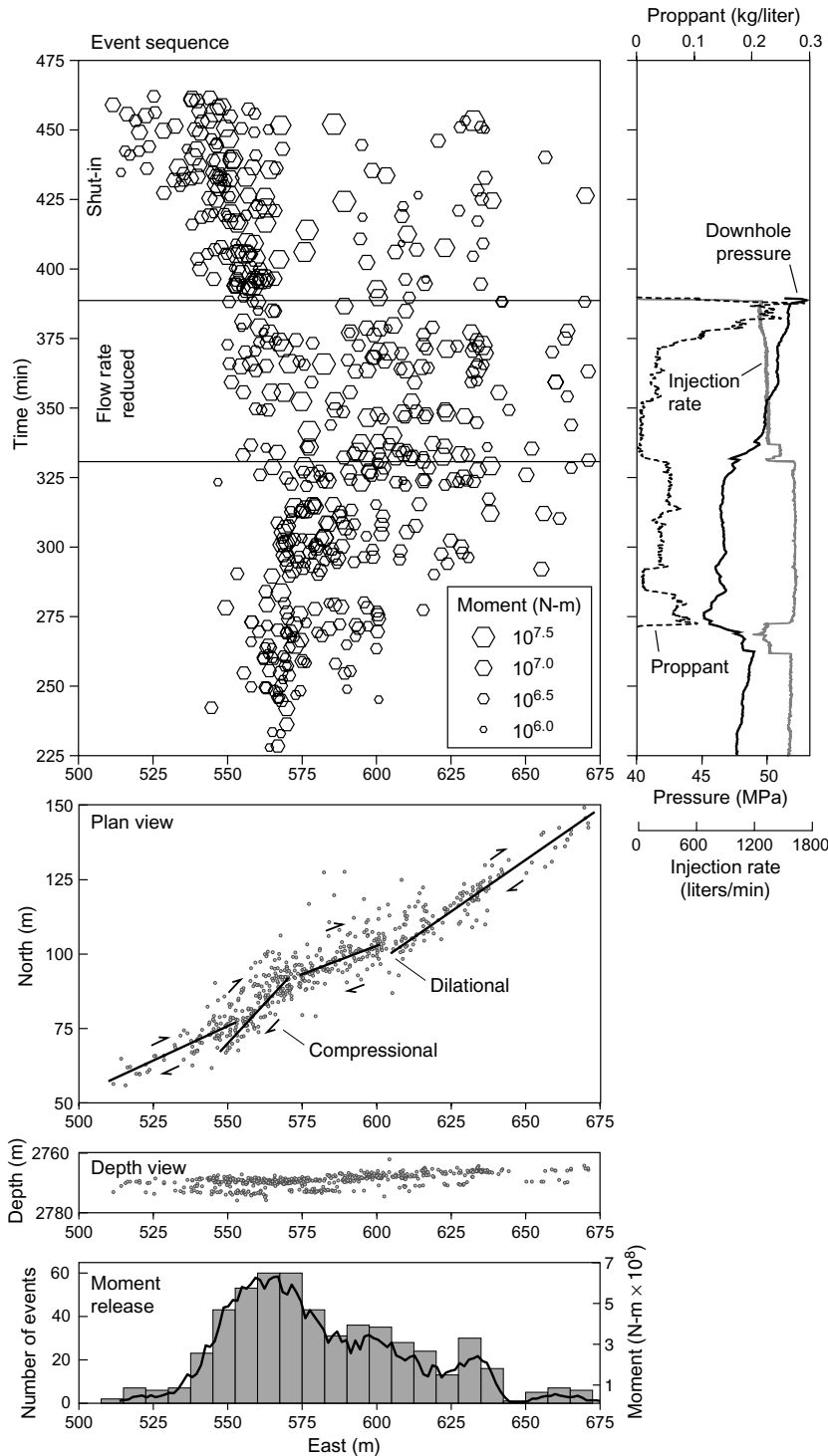


Figure 8. Location and growth details of cluster 5 of treatment E (Fig. 6). On the left are the moment and event-count distributions, depth and plan view of locations, and the time sequence of events, all plotted against the source's west-east positions. Moments are summed over a 10-m window, incremented at 1.5-m shifts. Symbols in the event sequence are proportional to $\log M_0$. The treatment data to the right are plotted versus the same time axis shown in the event sequence. The treatment well, 21-09, is located at about 335 m east (Fig. 6).

locations diverging in time, forming patterns that suggest the expulsion of fluids from compressive fault jogs. In Figure 11 we schematically illustrate our interpretation of the deformation and seismicity sequences induced by fluids being forced along such a natural structure. The jog area may initially be most active (Fig. 11a) because its orientation makes it more pressure sensitive for slip, and because stress is transferred by slip along the path of injection and builds at the

jog, as evident from the stationary, repetitive ruptures (e.g., Figs. 8–10). Pore pressure within the jog will increase locally due to the continued slip-induced loading (Nemcok *et al.*, 2002). Injection should resist the tendency for the jog to close, but once injection stops or is locally reduced, for instance by proppant buildup, the jog becomes a secondary fluid source with closure forcing fluids out (Fig. 11b). The pattern of seismicity then diverges from the jog as slip is

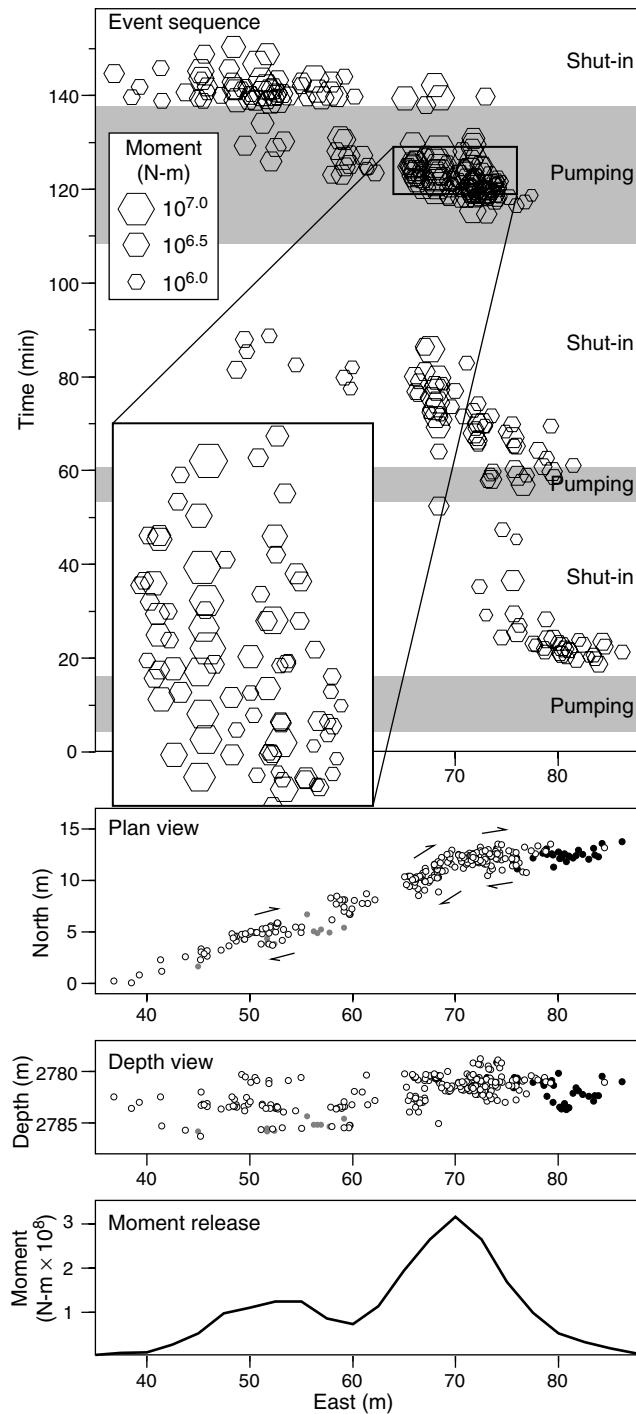


Figure 9. Location and growth details of cluster 4 of treatment B (Fig. 4). As on the left side of Figure 8, all displays are plotted against west-east source positions. Moments are summed over 10-m window, incremented at 2.5-m shifts. The shaded intervals of the event sequence are periods of injection, held constant at 106 l/sec. These are the first three pumping stages of treatment B, during which only treated water is injected. The symbols in the plan and depth views distinguish similar-waveform events. The distinction was observed as a slight change in *S*-waveform character on array 1. Right-lateral strike slip is induced along this fracture zone.

induced by the fluid forced out along the adjacent legs, slip that further drives the structure into compression, tending to lock up and concentrate stress at the jog (Fig. 11b). Faulting under higher mean stress is supported by fewer but larger events populating the jog or kink structures as treatments progress. This pattern can persist well after shut-in (Fig. 11c). Proppant buildup and screenout at these discontinuities will aggravate the problem of forming a choke point, further impeding proppant transport and fracture extension (Warpinski and Teufel, 1987). So, though the fluid flow forced by the slip-induced loading may appear to lengthen the treatment, as inferred from the seismicity extending past compressive fault jogs, the effective drainage lengths from the treatment well may be shorter.

On the positive side, the weaker, on-trend events outline the greater extent of the treatments and should be associated with fractures oriented near optimum for flow. Hydraulic extension of these shear fractures will result in linking natural and hydraulic fractures in a series of low-angle dilational jogs, which we have illustrated schematically as a narrow fracture mesh in Figure 12, similar to the mesh network proposed by Tezuka and Niitsuma (2000). Fracture opening and shearing will be closely coupled in such a system. Shearing tends to transfer through dilational jogs with opening along the jog equal to the transmitted slip (Segall and Pollard, 1980; Sibson, 1986). Conversely, hydraulic opening of the jogs will transfer to shear along the echelon fracture legs (Keer and Chen, 1981). In fact, shearing driven by opening of vertical hydraulic fractures may help explain our observations of strike-slip faulting along fractures with low resolved shear stress, and in what is likely a normal-faulting stress regime (see Rutledge and Phillips [2003] for summary of stress-regime information). Shearing linked with fracture opening will self-prop and sustain the volume increase. The equivalence of $\Delta M_0/\Delta V$ while activating the on-trend fracture systems implies that the fracture dilation sustained by the detected events was equal for a given volume injected, independent of the fluid types and flow rates used (e.g., treatments A and C + D of Fig. 7).

Analog to Creeping Sections of the San Andreas Fault?

Several features of the UCV microseismicity are similar to the small earthquakes that populate the San Andreas fault near Parkfield and San Juan Bautista, California, where slip occurs largely aseismically. These features include (1) horizontal banding of events trending parallel to the direction of slip (Rubin *et al.*, 1999), (2) event counts and moment release dominated by small patches of repetitive, periodic events (Nadeau *et al.*, 1995), and (3) diverging time-space patterns of locations that are attributed to fluid flow (Johnson and McEvilly, 1995). The similarities with our injection-induced seismicity lends support to Johnson and McEvilly's (1995) interpretation of fluid-driven slip near Parkfield. The dense patches of repetitive seismicity near Parkfield have been interpreted as localized zones of strength or stress con-

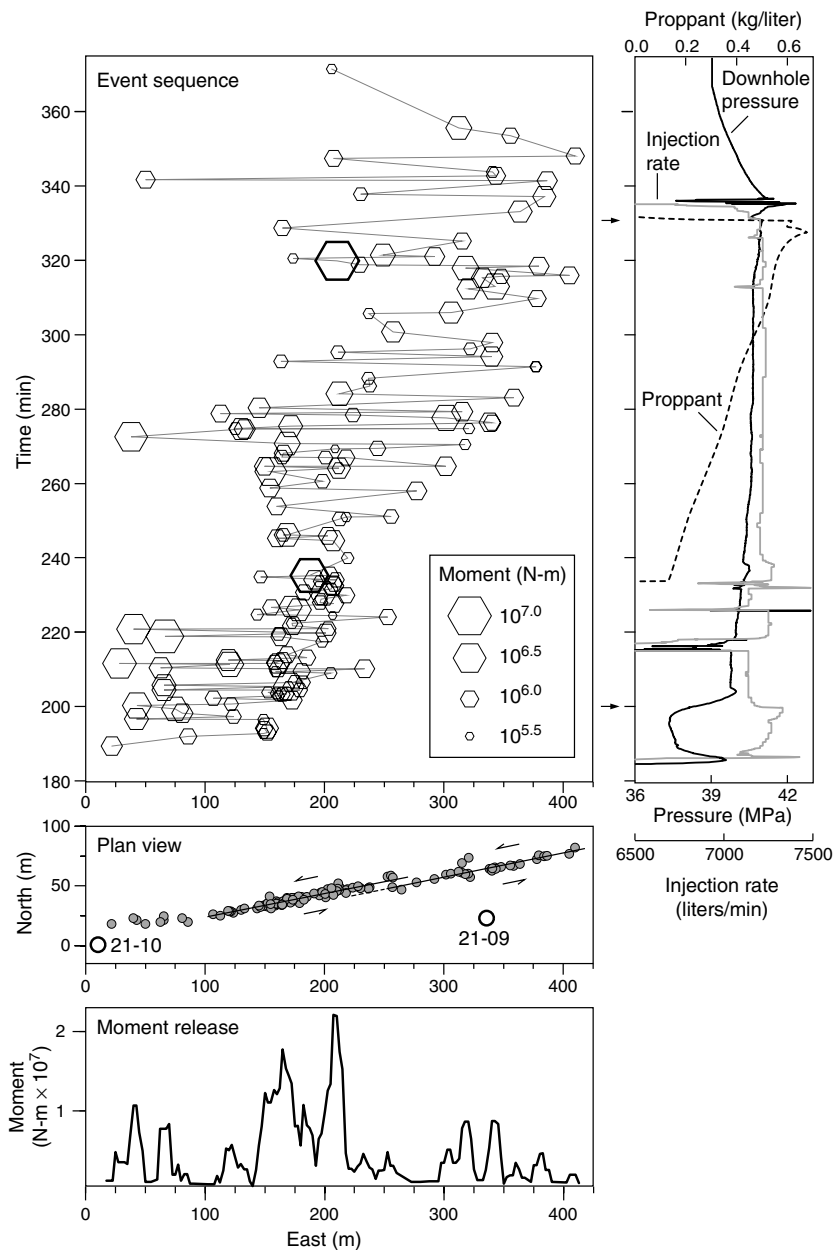


Figure 10. Location and growth details of a depth subcluster of treatment A, marked by the arrow in Figure 2. As on the left side of Figure 8, all displays are plotted against west-east source positions. Moments are summed over 10-m window, incremented at 2.5-m shifts. Ninety percent of these events fit a left-lateral strike slip mechanism (Fig. 3). The parallel lines, shown on each side of the trend offset near 250 m east, are best-fit linear regressions for events between 100 and 250 m and events greater than 250 m east. The trend offset is about 6 m. The two arrows along the treatment-data time axis mark the interval when the cross-linked gel was being injected.

centration, surrounded by larger regions undergoing stable, aseismic slip (Nadeau *et al.*, 1995). The similar features associated with structural heterogeneities within the UCV also suggest that a component of aseismic slip is induced, an interpretation that accords with our large moment deficits. Evans *et al.* (1999) noted that shear displacements inferred from source parameters of hydraulic-fracture seismicity are typically too small (<0.1 mm) to create significant permeability by shear dilation in terms of laboratory measurements of fracture-surface mismatches. Based in part on the results of Scotti and Cornet (1994) and Cornet *et al.* (1997), showing evidence for aseismic slip induced by fluid injections into granite, Evans *et al.* (1999) further suggested that the dislocation of larger-scale discontinuities by aseismic slip-page likely plays the most significant role in improving res-

ervoir permeability during hydraulic-fracture stimulation. Our inference of aseismic slip in the Carthage field supports their assertion.

The tie with Rubin *et al.*'s (1999) horizontal bands of seismicity observed further north near San Juan Bautista is less clear. They infer that the banded seismicity along the San Andreas is associated with relatively strong intervals between weak zones that simultaneously undergo aseismic slip. In our case, we are uncertain whether hydraulic fractures propagated aseismically through the intervening shales. Tracer logs indicate that most of the slurry was contained within the sands (Rutledge and Phillips, 2003), consistent with the seismic activation of a fracture system optimally oriented for flow and already contained within the target sands. But some slurry was also detected between the per-

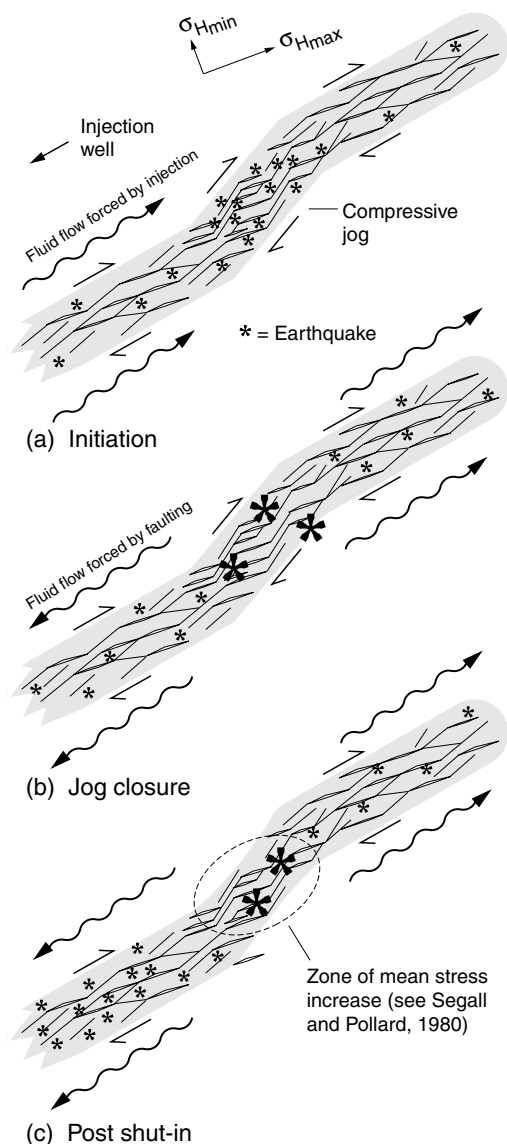


Figure 11. Plan-view schematic showing the sequence of deformation and seismicity induced by fluid injected along a portion of a narrow, preexisting fracture zone (shaded area) that forms a compressional jog. The injection well would be to the left of the figure, aligning with the fracture zone. The larger earthquake symbols represent larger magnitude events. Time progresses top to bottom. See text for a description of the sequence.

forated intervals, which is ambiguous due to the likely occurrence of flow behind casing. Some small-scale vertical communication is evident from the seismicity, such as the step feature near 65 m east in the depth view of Figure 9. Like the dominant flow paths, the inferred aseismic slip may also occur largely within the sands, as evident by large horizontal gaps in the seismicity that persist or develop in time (e.g., Figs. 6 and 11, respectively). If there is any analogy with the San Andreas bands, perhaps the UCV injections could be considered a snapshot wherein the relatively strong

zones of the San Andreas fault (more rigid and, hence, supporting fracture permeability) are weakened by preferential fluid invasion.

Summary

Hydraulic fracturing in the UCV is largely controlled by natural fractures isolated within the targeted sands, resulting in long, narrow fingers of stimulated rock. We envision the prevalent natural fracture system, known to be oriented close to hydraulic-fracture orientation, to be fairly discontinuous within a given sand layer. Stimulation improves connection by hydraulic extension and intersection, resulting in a mesh network of low-angle dilational jogs. Shearing on the natural fractures accompanying adjacent extension enhances and sustains the volume increases. A significant component of the shearing induced may occur aseismically. Some fracture offsets or orientation changes are encountered and pressurized, and these tend to concentrate stress and choke off fluid flow. Although these structural heterogeneities cannot be avoided, the adverse effects of impeding proppant transport and fracture growth at such features may be lessened with lower proppant concentrations.

Acknowledgments

Many thanks to Andi Kron for help with illustrations. We thank Keith Evans, Wayne Pennington, Jim Albright, Leo Eisner, Rick Sibson, and Don Dreesen for discussions and suggestions to improve the manuscript. This work has also benefitted from numerous discussions and presentations made through Professor Hiroaki Niitsuma's MTC International Collaborative Project, supported by NEDO. Funding was provided by the Gas Technology Institute and the U.S. Department of Energy's National Petroleum Technology Office.

References

- Albright, J. N., and C. F. Pearson (1982). Acoustic emissions as a tool for hydraulic fracture location: experience at the Fenton Hill Hot Dry Rock site, *Soc. Petro. Eng. J.*, August, 523–530.
- Andrews, D. J. (1986). Objective determination of source parameters and similarity of earthquakes of different size, in *Earthquake Source Mechanics*, S. Das, J. Boatwright, and C. H. Scholz (Editors), Geophysical Monograph 37, American Geophysical Union, Washington, D.C., 259–267.
- Andrews, D. J. (1989). Mechanics of fault junctions, *J. Geophys. Res.* **94**, 9389–9397.
- Birch, F. (1966). Compressibility: elastic constants, in *Handbook of Physical Constants*, Revised Ed., S. P. Clark, Jr. (Editor), Geol. Soc. Am. Memoir 97, New York, 97–173.
- Brune, J. N. (1968). Seismic moment, seismicity, and rate of slip along major fault zones, *J. Geophys. Res.* **73**, 777–784.
- Cornet, F. H., J. Helm, H. Poitrenaud, and A. Etchecopar (1997). Seismic and aseismic slips induced by large-scale fluid injections, *Pure Appl. Geophys.* **150**, 563–583.
- Dutton, S. P., S. E. Laubach, R. S. Tye, and T. N. Diggs (1991). Geological analysis of the Travis Peak formation and Cotton Valley sandstone, in *Staged Field Experiments No. 3: Application of Advanced Technologies in Tight Gas Sandstones—Travis Peak and Cotton Valley Formations, Waskom Field, Harrison County, Texas*, Gas Research Institute Report GRI-91/0048.
- Dyer, B. C., R. H. Jones, J. F. Cowles, O. Barkved, and P. G. Folstad (1999).

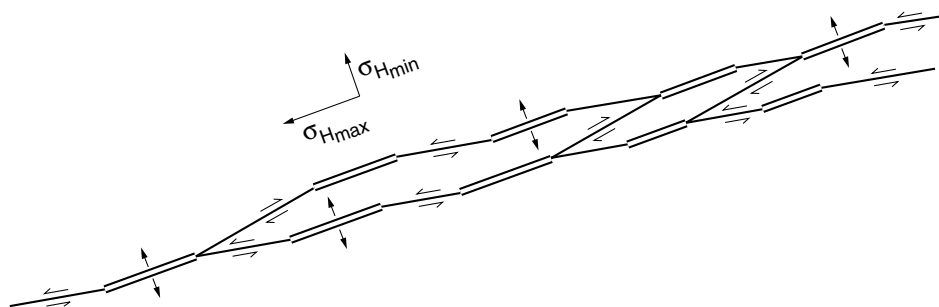


Figure 12. Plan-view schematic of a narrow, on-trend fracture mesh formed by a series of extensional (hydraulic) fractures connecting natural shear fractures. The single-line segments represent the natural fractures and are shown rotated $\pm 10^\circ$ from σ_{Hmax} . The double lines represent the hydraulic fractures. The predominant natural fracture orientation is slightly clockwise of σ_{Hmax} (undergoing left-lateral slip); these form a series of dilational jogs with the extensional fractures. Shearing along the natural fractures will result in an opening component along the extension fractures. Conversely, hydraulic opening of the jogs will transfer to a shear component along the echelon, natural fracture legs.

- Microseismic survey of a North Sea reservoir, *World Oil*, March, 74–78.
- Evans, K. F., F. H. Cornet, T. Hashida, K. Hayashi, T. Ito, K. Matsuki, and T. Wallroth (1999). Stress and rock mechanics issues of relevance to HDR/HWR engineered geothermal systems: review of developments during the past 15 years, *Geothermics* **28**, 455–474.
- Fehler, M., and W. S. Phillips (1991). Simultaneous inversion for Q and source parameters of microearthquakes accompanying hydraulic fracturing in granitic rock, *Bull. Seism. Soc. Am.* **81**, 553–575.
- Fehler, M., A. Jupe, and H. Asanuma (2001). More than cloud: new techniques for characterizing reservoir structures using induced seismicity, *The Leading Edge* **20**, 324–328.
- Gidley, J. L., S. A. Holditch, D. E. Nierode, and R. W. Veatch, Jr. (1989). Recent advances in hydraulic fracturing, SPE Monograph, Vol. 12, Society of Petroleum Engineers, Richardson, Texas.
- Griffin, L. G., R. B. Sullivan, S. L. Wolhart, C. K. Waltman, C. A. Wright, L. Weijers, and N. R. Warpinski (2003). Hydraulic fracture mapping of the high-temperature, high-pressure Bossier Sands in east Texas, in *Proc. 2003 Soc. Petro. Eng. Annu. Tech. Conf.*, Paper 84489, Denver, Colorado, 5–8 October 2003.
- House, L. (1987). Locating microearthquakes induced by hydraulic fracturing in crystalline rock, *Geophys. Res. Lett.* **14**, 919–921.
- Johnson, P. A., and T. V. McEvilly (1995). Parkfield seismicity: fluid driven?, *J. Geophys. Res.* **100**, 12,937–12,950.
- Jones, R. H., A. Beauce, A. Jupe, H. Fabriol, and B. C. Dyer (1995). Imaging induced microseismicity during the 1993 injection test at Soultz-sous-Forêts, France, in *Proc. World Geotherm. Cong.*, Florence, Italy, 18–31 May 1995, 2665–2669.
- Keck, R. G., and R. J. Withers (1994). A field demonstration of hydraulic fracturing for solid waste injection with real-time passive seismic monitoring, in *Proc. 1994 Soc. Petro. Eng. Annu. Tech. Conf.*, Paper 28495, New Orleans, Louisiana, 25–28 September 1994.
- Keer, L. M., and S. H. Chen (1981). The intersection of a pressurized crack with a joint, *J. Geophys. Res.* **86**, 1032–1038.
- Laubach, S. E. (1988). Subsurface fractures and their relationship to stress history in east Texas basin sandstone, *Tectonophysics* **156**, 37–49.
- Laubach, S. E., and E. R. Monson (1988). Coring-induced fractures: indicators of hydraulic fracture propagation in a naturally fractured reservoir, in *Proc. 1988 Soc. Petro. Eng. Annu. Tech. Conf.*, Paper 18164, Houston, Texas, 2–5 October 1988.
- McGarr, A. (1976). Seismic moment and volume change, *J. Geophys. Res.* **81**, 1487–1494.
- Maxwell, S. C., T. I. Urbancic, N. Steinsberger, and R. Zinno (2002). Microseismic imaging of hydraulic fracture complexity in the Barnett Shale, in *Proc. 2002 Soc. Petro. Eng. Annu. Tech. Conf.*, Paper 77440, San Antonio, Texas, 29 September–2 October 2002.
- Mayerhofer, M. J., and D. N. Meehan (1998). Waterfracs: results from 50 Cotton Valley wells, in *Proc. 1998 Soc. Petro. Eng. Annu. Tech. Conf.*, Paper 49104, New Orleans, Louisiana, 27–30 September 1998.
- Mayerhofer, M. J., M. F. Richardson, R. N. Walker, Jr., D. N. Meehan, M. W. Oehler, and R. R. Browning, Jr. (1997). Proppants? We don't need no proppants, in *Proc. 1997 Soc. Petro. Eng. Annu. Tech. Conf.*, Paper 38611, San Antonio, Texas, 5–8 October 1997.
- Mayerhofer, M. J., R. N. Walker, Jr., T. Urbancic, and J. T. Rutledge (2000). East Texas Hydraulic Fracture Imaging Project: measuring hydraulic fracture growth of conventional sandfracs and waterfracs, in *Proc. 2000 Soc. Petro. Eng. Annu. Tech. Conf.*, Paper 63034, Dallas, Texas, 1–4 October 2000.
- Moriya, H., H. Niituma, and R. Baria (2003). Multiplet-clustering analysis reveals structural details within the seismic cloud at the Soultz geothermal field, France, *Bull. Seism. Soc. Am.* **93**, 1606–1620.
- Nadeau, R. M., W. Foxall, and T. V. McEvilly (1995). Clustering and periodic recurrence of microearthquakes on the San Andreas fault at Parkfield, California, *Science* **267**, 503–507.
- Nemcok, M., A. Henk, R. A. Gayer, S. Vandycke, and T. M. Hathaway (2002). Strike-slip fault bridge fluid pumping mechanism: insights from field-based paleostress analysis and numerical modelling, *J. Struct. Geol.* **24**, 1885–1901.
- Pennington, W. D., S. D. Davis, S. M. Carlson, J. Dupree, and T. E. Ewing (1986). The evolution of seismic barriers and asperities caused by the depressuring of fault planes in oil and gas fields of south Texas, *Bull. Seism. Soc. Am.* **76**, 939–948.
- Pine, R. J., and A. S. Batchelor (1984). Downward migration of shearing in jointed rock during hydraulic injections, *Int. J. Rock Mech. Min. Sci. Geomech. Abstr.* **21**, 249–263.
- Phillips, W. S. (2000). Precise microearthquake locations and fluid flow in the geothermal reservoir at Soultz-sous-Forêts, France, *Bull. Seism. Soc. Am.* **90**, 212–228.
- Phillips, W. S., L. S. House, and M. C. Fehler (1997). Detailed joint structure in a geothermal reservoir from studies of induced microearthquake clusters, *J. Geophys. Res.* **102**, 11,745–11,763.
- Phillips, W. S., T. D. Fairbanks, J. T. Rutledge, and D. W. Anderson (1998). Induced microearthquake patterns and oil-producing fracture systems in the Austin Chalk, *Tectonophysics* **289**, 153–169.
- Rowe, C. A., R. C. Aster, W. S. Phillips, R. H. Jones, B. Borchers, and M. C. Fehler (2002). Using automated, high-precision repicking to improve delineation of microseismic structures at the Soultz geothermal reservoir, *Pure Appl. Geophys.* **159**, 563–596.

- Rubin, A. M., D. Gillard, and J. L. Got (1999). Streaks of microearthquakes along creeping faults, *Nature* **400**, 635–641.
- Rutledge, J. (1998). Analyses of the Cotton Valley microseismic data for asymmetric fracture growth, in *Cotton Valley Hydraulic Fracture Imaging and Waterfrac Projects, Data and Information Archive, Project Phases I, II, III and IV*, Gas Research Institute, Report No. GRI-99/0269.
- Rutledge, J. T., and W. S. Phillips (2003). Hydraulic stimulations of natural fracture as revealed by induced microearthquakes, Carthage Cotton Valley gas field, east Texas, *Geophysics* **68**, 441–452.
- Rutledge, J. T., W. S. Phillips, and B. K. Schuessler (1998). Reservoir characterization using oil-production-induced microseismicity, Clinton County, Kentucky, *Tectonophysics* **289**, 129–152.
- Scholz, C. H. (1990). *The Mechanics of Earthquakes and Faulting*, Cambridge University Press, Cambridge, 282–284.
- Scotti, O., and F. H. Cornet (1994). In situ evidence for fluid-induced aseismic slip events along fault zones, *Int. J. Rock Mech. Min. Sci. Geomech. Abstr.* **31**, 347–358.
- Segall, P., and D. D. Pollard (1980). Mechanics of discontinuous faults, *J. Geophys. Res.* **85**, 4337–4350.
- Sibson, R. H. (1981). Fluid flow accompanying faulting: field evidence and models, in *Earthquake Prediction: An International Review*, Maurice Ewing, Vol. 4, D. W. Simpson and P. G. Richards (Editors), American Geophysical Union, Washington D.C., 593–603.
- Sibson, R. H. (1986). Rupture interaction with fault jogs, in *Earthquake Source Mechanics*, S. Das, J. Boatwright, and C. H. Scholz (Editors), Geophysical Monograph 37, American Geophysical Union, Washington, D.C., 157–167.
- Sibson, R. H. (2001). Seismogenic framework for hydrothermal transport and ore deposition, *Soc. Econ. Geol. Rev.* **14**, 25–50.
- Snoke, J. A. (2003). FOCMEC: FOCal MEchanism determinations, in *International Handbook of Earthquake and Engineering Seismology*, W. H. K. Lee, H. Kanamori, P. C. Jennings, and C. Kisslinger (Editors), Academic Press, San Diego, Chapter 85.12.
- Tezuka, K., and H. Niitsuma (2000). Stress estimated using microseismic clusters and its relationship to fracture systems of the Hijiori hot dry rock reservoir, *Eng. Geol.* **56**, 47–64.
- Urbancic, T. I., and J. Rutledge (2000). Using microseismicity to map Cotton Valley hydraulic fractures, in *70th Annu. Mtg. Soc. of Explor. Geophys., Expanded Abstracts*, 6–11 August 2000, 1444–1448.
- Walker, R. N., Jr. (1997). Cotton Valley Hydraulic Fracture Imaging Project, in *Proc. 1997 Soc. Petro. Eng. Annu. Tech. Conf.*, Paper 38577, San Antonio, Texas, 5–8 October 1997.
- Warpinski, N. R., and L. W. Teufel (1987). Influence of geologic discontinuities on hydraulic fracture propagation, *J. Petro. Technol.* **39**, 209–220.
- Warpinski, N. R., P. T. Branagan, R. E. Peterson, S. L. Wolhart, and J. E. Uhl (1998). Mapping hydraulic fracture growth and geometry using microseismic events detected by a wireline retrievable accelerometer array, in *Proc. 1998 Soc. Petro. Eng. Gas Tech. Symp.*, Paper 40014, Calgary, Alberta, Canada, 15–18 March 1998.
- Zhang, X., and D. J. Sanderson (1996). Numerical modelling of the effects of fault slip on fluid flow around extensional faults, *J. Struct. Geol.* **18**, 109–119.

Los Alamos National Laboratory
 Los Alamos, New Mexico 87545
 jrutledge@lanl.gov
 (J.T.R., W.S.P)

Pinnacle Technologies, Inc.
 Houston, Texas 77090
 (M.J.M.)

Manuscript received 22 December 2003.